Research Article

In-situ synthesis of gadolinium niobate quasi-binary composites with balanced mechanical and thermal properties for thermal barrier coatings

Yi HAN[a], Peng-an ZONG[a], Muzhang HUANG[a], Zesheng YANG[a], Yingjie FENG[a], Wei PAN[a], Peng ZHANG[a,b,*], Chunlei WAN[a,*]

[a]*State Key Laboratory of New Ceramics and Fine Processing, School of Materials Science and Engineering, Tsinghua University, Beijing 100084, China*
[b]*Institute of Welding and Surface Engineering Technology, Faculty of Materials and Manufacturing, Beijing University of Technology, Beijing 100124, China*

Abstract: Yttria-stabilized zirconia (YSZ) has been used as a thermal barrier coating (TBC) material in gas turbines for several decades. Although continuous efforts have been made to develop novel TBC materials that can work at a higher temperature, no single material other than YSZ has all the desired attributes for the TBCs. In this paper, we report the *in-situ* synthesis of quasi-binary $GdNbO_4/Gd_3NbO_7$ composites based on the simple Gd_2O_3–Nb_2O_5 binary phase diagram. The fracture toughness of these quasi-binary composites is remarkably enhanced compared with the value predicted by the rule of mixtures because the ferroelastic domain switching is more activated due to the residual stress in the quasi-binary composites, which triggers more crack defections due to the enlarged process zone. Additionally, the Gd_3NbO_7 phase provides a low thermal conductivity due to the substantial chemical inhomogeneity, which diffuses phonons. $Gd_3NbO_7/GdNbO_4$ exhibits a balanced thermal conductivity of 1.6 W/(m·K) at 1073 K and a toughness value of 2.76 MPa·m$^{0.5}$, and these values are among the best comprehensive properties that have been obtained for new TBC materials. The work demonstrates a feasible approach of designing a new TBC material with balanced properties and can be easily fabricated.

Keywords: thermal barrier coating (TBC); fracture toughness; thermal conductivity; residual stress

1 Introduction

Thermal barrier coating (TBC) systems were developed to protect the hot-section components of gas turbine engines and have been in use for several decades. They can provide a temperature gradient across the ceramic topcoat, thereby allowing the metallic substrate to be used at elevated temperatures. The state-of-the-art ceramic topcoat material is yttria-stabilized zirconia (YSZ) of 6–8 wt%, which consists of metastable tetragonal phase zirconia (*t'*-ZrO$_2$). *t'*-ZrO$_2$ presents good overall properties under 1473 K, including good thermal properties, chemical stability, and mechanical properties [1,2]. However, as there is still an urgent demand for the

---

ability to increase the inlet temperatures to increase the thermal efficiency of the gas turbine engines [3–5], YSZ cannot fulfil this requirement since the phase transformation of the *t'* phase above 1473 K would cause severe coating spallation. Additionally, the sintering behaviour of YSZ occurs at higher temperatures, inducing thermal stresses during the application and accelerating the failure of the TBC system [6,7]. As the development of a cooling system and substrate superalloy materials for the TBC systems has already met a bottleneck, the most feasible way to boost the inlet temperatures is to explore new ceramic topcoat materials. Research efforts exploring new ceramic topcoat materials are mainly focused on two categories: multiple oxide-stabilized ZrO_2 and new materials [8–11]. To date, many kinds of materials have been studied as promising ceramic topcoat materials, such as $RE_2Zr_2O_7$ (RE = rare earth) [12–14], mullite [15], RE_2SiO_5 [16], $REPO_4$ [17], $RETi_2Al_9O_{19}$ [18,19], hexaaluminate [20], and perovskites [21]. Compared with the traditional material YSZ, these new materials usually have better thermal stability and lower thermal conductivities. However, YSZ still cannot be completely replaced, as these new materials always exhibit a low fracture toughness with a low resistance to crack propagation throughout their service lifetime. Recently, a new group of materials, which includes $RETaO_4$ and $RENbO_4$, has been intensively studied [22–25], and these materials have ferroelastic characteristics similar to YSZ. It could offer an additional high-temperature toughening mechanism, contributing to a higher fracture toughness. However, these tantalates and niobates always show a relatively high thermal conductivity. Our recent work [26] has indicated that RE_3NbO_7 is a promising group of ceramic topcoat materials, which has low thermal conductivities, high thermal stability, and excellent oxygen resistance. However, the low fracture toughness restricts the application of the RE_3NbO_7 series. Therefore, although there have been numerous reports on the development of new TBC materials, no single material aside from YSZ that has all the desired attributes for the TBCs has been reported, especially with balanced mechanical and thermal properties.

In this paper, to combine the high mechanical properties of $RENbO_4$ and good thermal properties of RE_3NbO_7, we report quasi-binary $GdNbO_4/Gd_3NbO_7$ composites for potential TBC applications based on the coexistence region in the binary phase diagram of Gd_2O_3 and Nb_2O_5 (Fig. S1 in the Electronic Supplementary

Material (ESM)). The fracture toughness of the quasi-binary composites is not a simple average of the two components, $GdNbO_4$ and Gd_3NbO_7. Instead, a 30%–40% improvement over the value calculated by the rule of mixtures is observed. The main reason for such improvement is the residual tensile strain in the quasi-binary compound, which activates more switching of the ferroelastic domain, as evidenced by the enlarged process zone and the increase in a crack deflection. The quasi-binary composites also show a low thermal conductivity of 1.6 W/(m·K) at 1073 K due to the Gd_3NbO_7 phase, in which the substantial chemical inhomogeneity strongly diffuses phonons. In contrast to other complex TBC materials whose compositions deviate greatly in the thermal spray process, the quasi-binary composites are synthesized *in-situ* from binary Gd_2O_3 and Nb_2O_5 powders, which may provide advantages in coating fabrication.

2　Experimental

The detailed sample preparation and measurements of the properties of ceramic $Gd_3NbO_7/GdNbO_4$ composites are described in the ESM.

3　Results and discussion

3.1　Phase composition

The XRD patterns of the $Gd_3NbO_7/GdNbO_4$ ceramic composites are presented in Fig. 1. The symbols of C1, C2, and C3 represent the samples with 30, 50, and 70 vol% of $GdNbO_4$ content, respectively. Figure 1(a) shows the XRD patterns of pure Gd_3NbO_7 and $GdNbO_4$, which are well matched with the standard JCPDS cards. Gd_3NbO_7 (0 vol%) exhibits a weberite-type structure with the space group Ccmm, and $GdNbO_4$ (100 vol%) displays a fergusonite-type structure with the space group I2(5). No additional phases are present; the only diffraction peaks in the XRD patterns of the $Gd_3NbO_7/$ $GdNbO_4$ ceramic composites are those corresponding to Gd_3NbO_7 and $GdNbO_4$, indicating that a chemical reaction between these two compounds did not occur. With increasing $GdNbO_4$ content, the intensity of the $GdNbO_4$ peaks in the composites increases gradually. The XRD results reveal that the $Gd_3NbO_7/GdNbO_4$ ceramic composites were synthesized successfully with good phase compatibility.
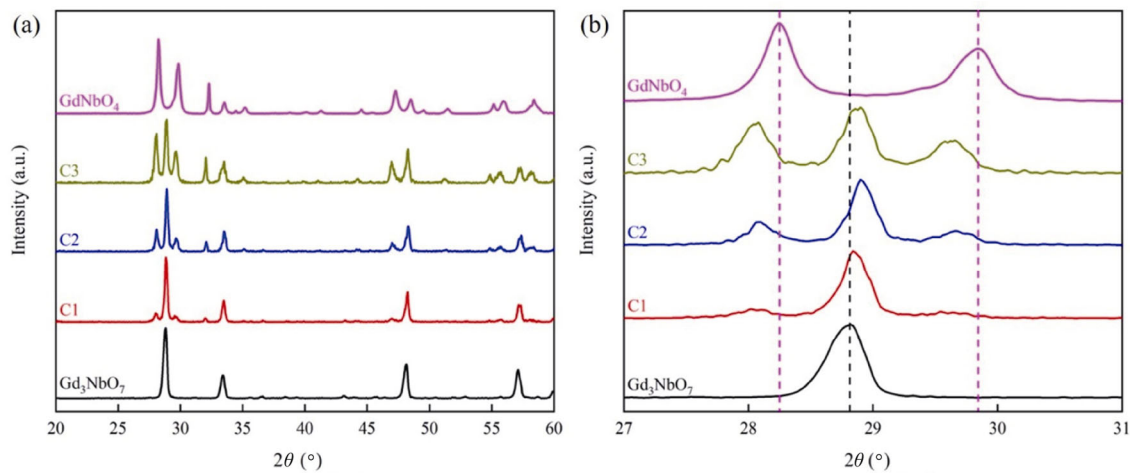
Fig. 1 XRD patterns of Gd$_3$NbO$_7$/GdNbO$_4$ composites: (a) 2θ ranging from 20° to 60° and (b) 2θ ranging from 27° to 31°.

Figure 1(b) shows the XRD patterns in the range of 27°–31°. As the content of GdNbO$_4$ increases, the peaks for GdNbO$_4$ shift slightly to small angles, while the peaks for Gd$_3$NbO$_7$ shift to large angles. The opposite shifts of the peaks are attributed to the stress state within the ceramic composites, which are induced by the mismatch of the coefficients of thermal expansion (CTEs) between Gd$_3$NbO$_7$ and GdNbO$_4$ [27]. Herein, the tensile stress is generated in GdNbO$_4$, which has a larger CTE, and paired compressive stress is present in Gd$_3$NbO$_7$, which has a smaller CTE.

The scanning electron microscopy (SEM) micrograph with the backscattered electron mode (BSE) of the thermal-etched surface of the Gd$_3$NbO$_7$/GdNbO$_4$ composites is shown in Fig. S2 in the ESM. Figures S2(a)–S2(e) in the ESM show that the dense ceramics with no observable pores were obtained. The Gd$_3$NbO$_7$ and GdNbO$_4$ grains were homogeneously mixed. The average size of the Gd$_3$NbO$_7$ grains decreased as a function of the GdNbO$_4$ content due to the pinning effect of the component phase particles. The detailed analysis is shown in the ESM. The gradual evolution of the biphasic microstructure could alter the interface state, residual stresses within the grains, and crack propagation path, which could greatly impact the mechanical properties of the quasi- binary Gd$_3$NbO$_7$/GdNbO$_4$ composites.
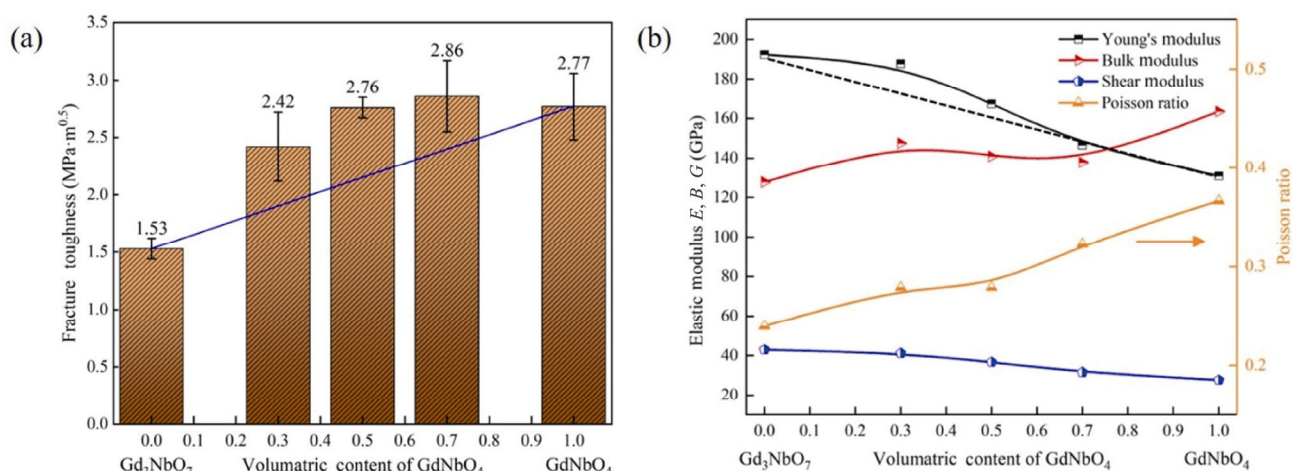
3. 2   Fracture toughness

The fracture toughness of the Gd$_3$NbO$_7$/GdNbO$_4$ composites was measured by the single edge notch beam (SENB) method shown in Fig. 2(a), and it increased with increasing GdNbO$_4$ content. Specifically, the pure Gd$_3$NbO$_7$ has a relatively low fracture toughness of approximately 1.53 ± 0.09 MPa·m$^{0.5}$, while GdNbO$_4$ has a high fracture toughness of approximately 2.77 ± 0.29 MPa·m$^{0.5}$. The maximum value of the ceramic composites was approximately 2.86 ± 0.31 MPa·m$^{0.5}$ for C3, which is much higher than those of most newly reported TBC materials. The blue line in Fig. 2(a) is the fracture toughness calculated by the rule of mixtures. Clearly, all the measured values of fracture toughness are larger than the calculated results. Compared with the fracture toughness values obtained from the mixture law, the real toughening values were corrected to be 33.65%, 39.84%, and 29.97% higher for C1, C2, and C3, respectively. This result implies that additional toughening mechanisms are involved in the ceramic composites. It is widely acknowledged that the high fracture toughness is beneficial for prolonging the lifetime of TBCs. Although many new candidate TBC materials have been reported to replace YSZ, such as RE$_2$Zr$_2$O$_7$ [28], RE$_3$NbO$_7$ [26], RETa$_3$O$_9$ [29], REPO$_4$ [30], SrZrO$_3$ [21], and Ba(Mg$_{1/3}$Ta$_{2/3}$)O$_3$ [31], the toughness values are quite low, in the range of 1–2 MPa·m$^{0.5}$. The high fracture toughness values in the Gd$_3$NbO$_7$/GdNbO$_4$ quasi-binary composites suggest that they are more resistant to the thermal mechanical stress in service with a potential longer lifetime.

To better understand the toughening mechanisms, the overall crack propagation of the ceramic composites was closely investigated, as shown in Figs. 3(a)–3(e). Figures 3(f)–3(k) present the specific crack propagation corresponding to the potential toughening mechanisms, which will be discussed in detail in Section 3.3.

3. 3   Toughening mechanisms

According to the results discussed above, we can confirm

Fig. 2 Mechanical properties of Gd_3NbO_7/$GdNbO_4$ composites: (a) fracture toughness of Gd_3NbO_7/$GdNbO_4$ composites measured by SENB method; and (b) measured Poisson ratio and calculated Young's modulus (E), bulk modulus (B), and shear modulus (G) of Gd_3NbO_7/$GdNbO_4$ composites.
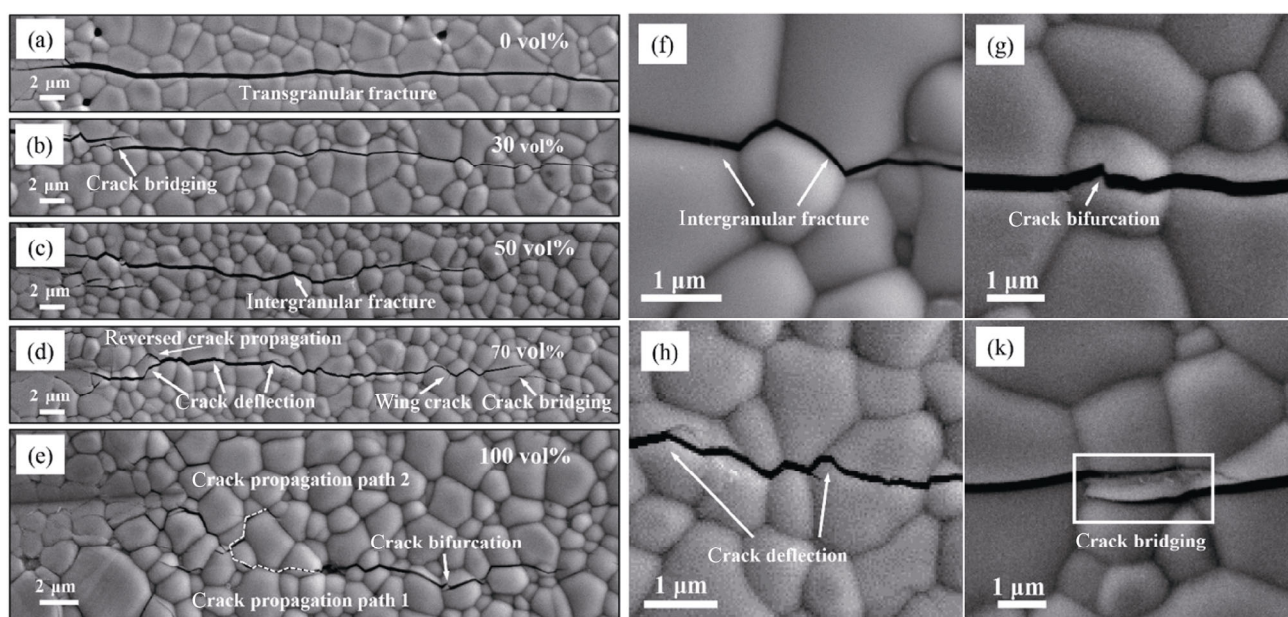
Fig. 3 Crack propagation path of Gd_3NbO_7/$GdNbO_4$ composites: (a) Gd_3NbO_7, (b) C1, (c) C2, (d) C3, and (e) $GdNbO_4$. Involved toughening mechanisms: (f) intergranular fracture, (g) crack bifurcation, (h) crack deflection, and (k) crack bridging.

that the fracture toughness of the ceramic composites was significantly enhanced. According to the microstructure of the composites and intrinsic properties of the components, the potential toughening mechanisms may include grain boundary toughening, ferroelastic toughening, residual stress toughening, and the synergistic effects of these mechanisms.

3.3.1 Grain boundary toughening

The grain boundary toughening of the Gd_3NbO_7/$GdNbO_4$ composites comes from the refinement of grain size and the switch from the transgranular fracture mode to the intergranular mode. In the pure Gd_3NbO_7, only the

transgranular crack was observed. With the addition of $GdNbO_4$, although the transgranular fracture still dominated the crack propagation of C1 (Fig. 3(b)), the crack bridging and intergranular fracture occurred during the crack propagation. As the $GdNbO_4$ content was increased to 50 vol%, the transgranular fracture no longer dominated the crack propagation of C2. More intergranular fracture was observed, as shown in Fig. 3(c). When the $GdNbO_4$ content was further increased to 70 vol%, more toughening mechanisms that could consume more fracture energy occurred. In Fig. 3(d), in addition to the crack bridging and intergranular fracture, the crack deflection and wing crack are also

observed. Moreover, reversed crack propagation, which occurs in the opposite direction of the propagation path of the main crack, was also observed. Such reversed crack is related to the crack bridging. In the preliminary stage of crack bridging, the propagation of the primary crack is impeded by the friction between grains, and the secondary crack develops. With the growth of secondary crack, the friction falls off. The primary crack grows and part of the secondary crack closes. The reversed crack is formed. A similar phenomenon was also found in Rödel's research [32]. The crack propagation of pure $GdNbO_4$, as shown in Fig. 3(e), is inclined to the intergranular fracture, which was discussed in our prior study [33]. The crack mode switched primarily due to the weakened interface between the dissimilar Gd_3NbO_7 and $GdNbO_4$ phases. While the length of crack propagation increased with more intergranular modes, the weakened interface energy may have resulted in a limited contribution to the enhancement of fracture toughness.

3.3.2 Ferroelastic toughening

In addition to the intergranular crack, the crack deflection also appeared inside the grains due to the presence of ferroelastic $GdNbO_4$ phases. The AFM images of the Gd_3NbO_7/$GdNbO_4$ composites shown in Fig. 4 exhibit different features of $GdNbO_4$ and Gd_3NbO_7 grains. In Fig. 4(a), a crack propagates through the $GdNbO_4$ grains and then propagates along with the Gd_3NbO_7/$GdNbO_4$ interface. The $GdNbO_4$ grains on the upper side of the crack have strip-like patterns regarded as ferroelastic domains, while the Gd_3NbO_7 grains on the lower left has a smooth surface. The ferroelastic domains in the $GdNbO_4$ grains next to the crack switched, enabling

them to consume more crack propagation energy to improve the fracture toughness. The related toughening mechanisms, including the crack bifurcation, crack bridging, crack deflection, and domain switching, can be observed in Figs. 4(a) and 4(b), with some of these corresponding to the crack propagation shown in Figs. 3(g) and 3(k).

The ferroelastic toughening can be easily understood through the domain state change under an external force. In perfect grains, the ferroelastic domains are evenly arranged with similar widths under no external force. Once encountering an external force, the domain state can change, not only through domain switching but also through the variation of domain density and domain width. All the above-mentioned variations in the domains can be easily observed in Figs. 4(a) and 4(b). The crack along the Gd_3NbO_7/$GdNbO_4$ interface in Fig. 4(a) reveals that the domain switching occurred next to the crack, and the domain density and width variation occurred away from the crack. The tensile stress normal to the direction of the crack propagation is present around the crack tip area. The tensile stress plays a key role in the shear stress, which can trigger the domain switching. When the shear stress exceeds the threshold, the domains start to switch to a direction that depends on the relative direction of ferroelastic domains to the crack propagation. The crack propagation within the $GdNbO_4$ grains also leads to the variation of domain density and width, which results in the crack bifurcation and deflection. As shown in Fig. 4(b), the variation in the domain state can also lead to the crack bridging during the propagation. In addition to these toughening mechanisms, the reversed crack propagation was also observed in C3, which is not
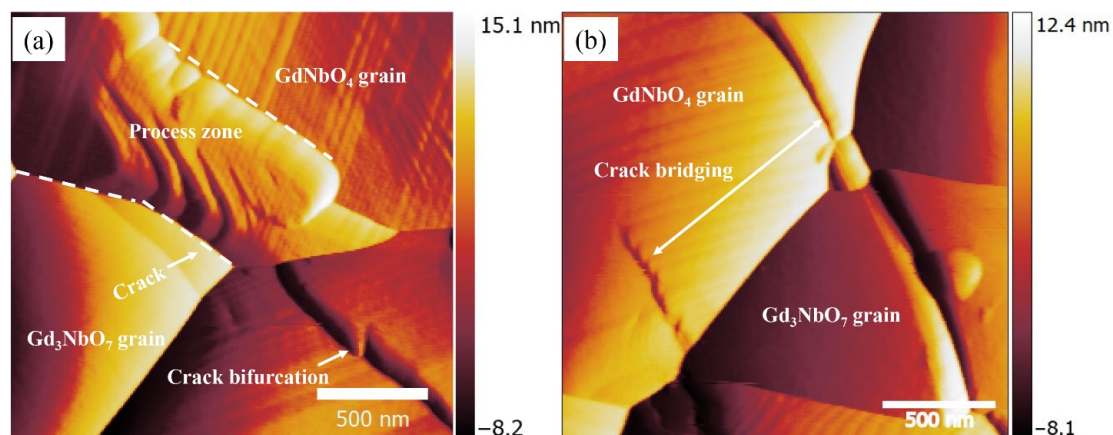
Fig. 4 AFM images around crack in Gd_3NbO_7/$GdNbO_4$ composites: (a) domain state observed by AFM and (b) crack bridging and deflection within the $GdNbO_4$ grains.

determined by a single toughening mechanism, possibly because the domain switching and weak bonding strength between the grains changed the propagation route. The variation in the domain state could absorb the crack propagation energy around the crack tip area to prevent the crack propagation, consequently improving the fracture toughness of the Gd_3NbO_7/$GdNbO_4$ composites.

3.3.3 Residual stress toughening

The stress state of the ceramic Gd_3NbO_7/$GdNbO_4$ composites is complicated due to the CTE mismatch when cooled from the fabrication temperature. In this work, the average CTEs of Gd_3NbO_7 and $GdNbO_4$ were calculated to be 9.3×10^{-6} and 10.1×10^{-6} K^{-1}, respectively, based on the measured CTEs. Thus, the paired compressive and tensile stress were generated within the Gd_3NbO_7 matrix and component phase $GdNbO_4$, respectively. The XRD analysis, which could measure the stress of an arbitrary direction in a small area through the $\sin^2\psi$ method, was used to measure the thermal residual stress [34,35]. The schematic diagram is shown in Fig. 5(a). The residual stress can be quantified by Eq. (1) [36]:

$$\sigma_\varphi = \left(\frac{E}{1+v}\right)\frac{1}{d_0}\left(\frac{\partial d_{\varphi\psi}}{\partial \sin^2\psi}\right) \tag{1}$$

where σ_φ is the residual stress, E is the Young's modulus, v is the Poisson's ratio, d_0 is the interplanar spacing in the free stress, and $d_{\varphi\psi}$ is the interplanar spacing measured in the direction defined by φ and ψ. The angel of ψ was selected in a range of $0°–30°$, and 2θ was selected in a range of $69.5°–72.0°$ for Gd_3NbO_7 and $50°–53°$ for $GdNbO_4$ to evaluate the residual stress of the Gd_3NbO_7/$GdNbO_4$ composites. The paired compressive and tensile stresses are plotted in Fig. 5(b)

based on the values of the parameters shown in Fig. 2(b) and the relationship between $d_{\varphi\psi}$ and $\sin^2\psi$ calculated by the XRD analysis. The value of the strain near the interface between two phases is decided by the mismatch of CETs, and decreases with the increase of the distance from the interface. Theoretically, the tensile stress within the $GdNbO_4$ grains decreases with increasing $GdNbO_4$ content, while the compressive stress within the Gd_3NbO_7 grains continuously increases. However, the compressive stress within the Gd_3NbO_7 grains increases firstly and then decreases in Fig. 5(b). One reason is the large error bar shown in the figure. If the error bar is considered, the compressive stress in Gd_3NbO_7 in the C2 sample is in fact comparable to the value in the C3 sample. The other reason is that with increasing $GdNbO_4$ content, the ferroelastic transition in $GdNbO_4$ could alleviate the internal strain, with a reduction of internal stress values [37,38]. Therefore, the stress value in Gd_3NbO_7 in the C3 sample with more $GdNbO_4$ content could be somewhat smaller than expected.

Mode I crack or opening crack is the most main and most dangerous fracture mode under in-plane loading in fracture mechanics [39]. In Mode I crack, the movement trend of crack surfaces is perpendicular to the crack line, and the crack propagation is directly related to the tensile stress perpendicular to the crack surface. In the C1 samples with a high content of Gd_3NbO_7, the compressive stress will offset the influence of the applied load when the crack tip propagates into the Gd_3NbO_7 phase. In the C3 samples, Gd_3NbO_7 acts as the second phase. The crack tends to bypass the Gd_3NbO_7 grains under the influence of compressive stress, and the crack deflection and bridging occur [40]. Therefore, the compressive stress in the Gd_3NbO_7
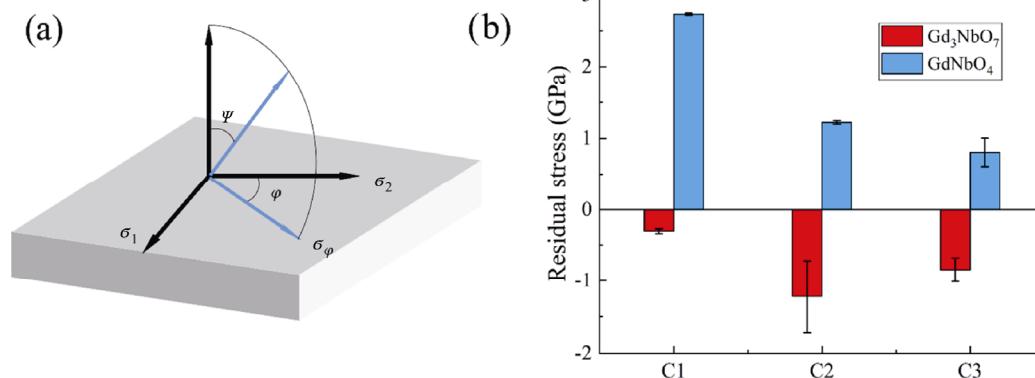
Fig. 5 XRD residual stress measurement: (a) schematic diagram and (b) calculated residual compressive stress and tensile stress within Gd_3NbO_7 and $GdNbO_4$.

phase could increase the fracture toughness. The influence of tensile stress is the opposite. However, in the ferroelastic materials, the tensile stress may have an entirely different effect. The ferroelastic domains are highly labile in tensile stress fields with a lower energy barrier for the domain switching [41]. As a result, the domain state changes more easily under an external force. Compared with those in our previous research, the $Gd_3NbO_7/GdNbO_4$ composites presented a wider process zone under the same experimental conditions, as shown in Fig. 6. This result indicates that more domain states in the stress field of the crack tip change, and the resistance of the crack propagation is further enhanced. The crack shown in Figs. 3(d) and 6(b) exhibit a zigzag shape with more crack deflection, demonstrating that more ferroelastic domain switching is activated with the assistance of tensile stress. Therefore, in the $Gd_3NbO_7/$ $GdNbO_4$ composites, the compressive stress in the Gd_3NbO_7 grains and the tensile stress in the $GdNbO_4$ grains both improved the fracture toughness of the materials.
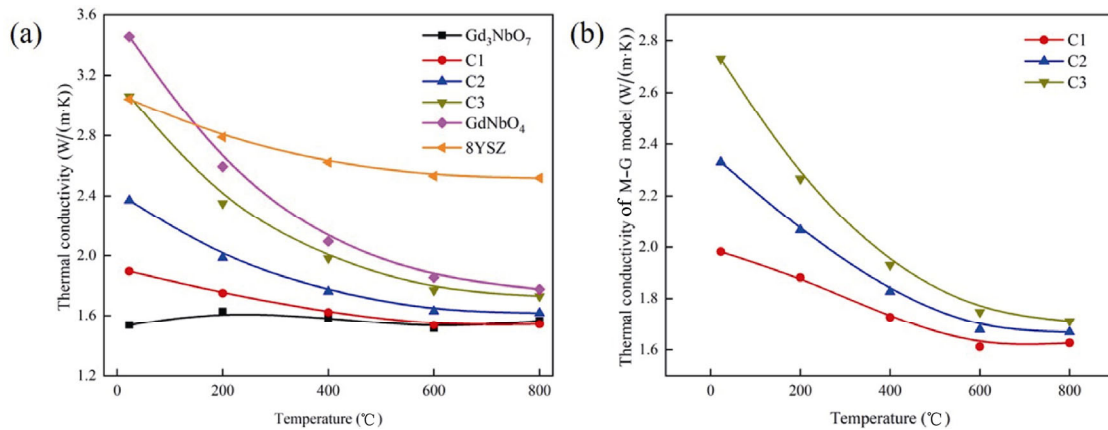
3. 4 Thermal conductivity

The thermal conductivities of the $Gd_3NbO_7/GdNbO_4$ composites were calculated by Eq. (S2) in the ESM, and the results are shown in Fig. 7(a). The thermal conductivities of pure Gd_3NbO_7 and $GdNbO_4$ displayed different variation tendencies at elevated temperatures. Gd_3NbO_7 exhibited glass-like thermal conductivities that increased slightly with increasing temperature, while $GdNbO_4$ exhibited a traditional thermal conductivity of crystalline materials following the $1/T$ law. The thermal conductivities of the ceramic composites were between those of the two pure materials. Specifically, the thermal conductivities of the ceramic composites increased with increasing $GdNbO_4$ content over the measured temperature range. C1 exhibited the lowest value of approximately 1.54 W/(m·K) at 800 ℃, which was even slightly lower than that of Gd_3NbO_7 (1.56 W/(m·K) at 800 ℃). Moreover, the characteristics of the crystalline thermal conductivities of ceramic composites became more obvious with increasing $GdNbO_4$ content. There was an apparent thermal conductivity interval between C2 and C3 at 800 ℃. The thermal conductivities of C1 and C2 are very close to that of Gd_3NbO_7, indicating that the introduction of the strengthening phase did not degrade their thermal insulation properties at a high temperature. Compared with the thermal conductivity
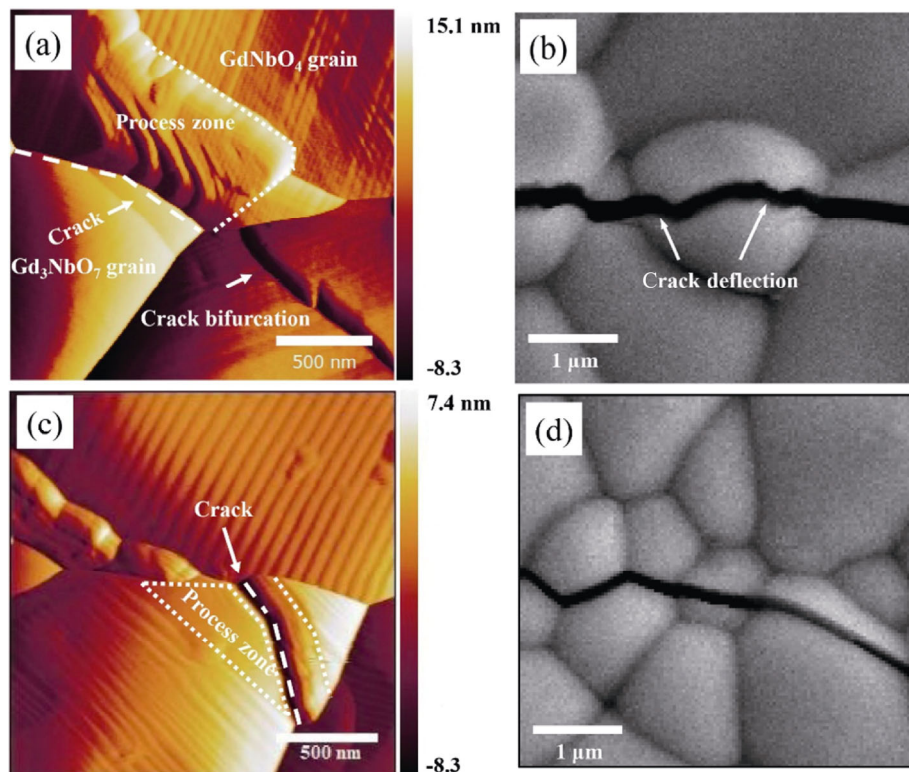
Fig. 6 Comparison of domain switching: (a) domain state of $Gd_3NbO_7/GdNbO_4$ composites observed by AFM; (b) crack deflection within the $GdNbO_4$ grains of $Gd_3NbO_7/GdNbO_4$ composites; (c) ferroelastic domain state in pure $GdNbO_4$ [33]; and (d) less crack deflection in pure $GdNbO_4$.

Fig. 7 Thermal properties of Gd$_3$NbO$_7$/GdNbO$_4$ composites: (a) thermal conductivity and (b) thermal conductivity calculated by Maxwell–Garnett (M–G) model.

of 8YSZ (2.7 W/(m·K), at 800 ℃ [42]), the thermal conductivities of all the above mentioned materials are much lower than that of 8YSZ. Meanwhile, they are also lower than those of many new TBC materials reported in literature, such as SrZrO$_3$ [21], REPO$_4$ [30], RETa$_3$O$_9$ [29], Ba(Mg$_{1/3}$Ta$_{2/3}$)O$_3$ [31], Ln$_2$Sn$_2$O$_7$ [43], Yb$_2$Zr$_2$O$_7$ [44], and RE$_2$Ce$_2$O$_7$ [45].

The thermal conductivities of Gd$_3$NbO$_7$/GdNbO$_4$ composites are mainly determined by the phonon scattering that relates to the mean free path of the phonon. Two main factors affect the phonon mean free path: intrinsic phonon scattering and phonon-imperfection scattering. The total phonon scattering can then be described by using Eq. (2) [46]:

$$\frac{1}{l(\omega,T)} = \frac{1}{l_i(\omega,T)} + \frac{1}{l_p(\omega)} + \frac{1}{l_b} \tag{2}$$

where $l_i(\omega,T)$, $l_p(\omega)$, and l_b represent the mean free path of the phonon derived from the intrinsic scattering, the point defect scattering, and the boundary scattering, respectively. As the grain size is several orders of magnitude larger than that of the mean free path of the phonon, the scattering caused by phonon-grain boundaries can be neglected. Thus, the thermal conductivities of Gd$_3$NbO$_7$/GdNbO$_4$ composites are dominated by the scattering caused by the intrinsic characteristics and point defects. Previous work [26,47] based on the series of RE$_3$NbO$_7$ (RE = rare earth) has proven that the point defects in Gd$_3$NbO$_7$, including cation antisite defects and oxygen vacancies, lead to intense phonon scattering. Moreover, the large intrinsic chemical inhomogeneity of rare-earth niobates (RE$_3$NbO$_7$), in terms of the charge disorder and fluctuation of bonding length, which we have already illustrated in another

work, can also cause intense phonon scattering [48]. As a result of the point defects and substantial chemical inhomogeneity, the scattering of vibrational modes is maximized, leading to lower thermal conductivities of ceramic composites.

The effective medium theory (EMT) and Green's function technique are usually used to predict the properties of composite materials. In this work, the M–G model (Eq. (3)) was used to evaluate the thermal conductivities of the ceramic composites [49]:

$$\frac{\kappa - \kappa_1}{\kappa + 2\kappa_1} = V\frac{\kappa_2 - \kappa_1}{\kappa_2 + 2\kappa_1} \tag{3}$$

where κ, κ_1, and κ_2 represent the thermal conductivities of the ceramic composites, Gd$_3$NbO$_7$ matrix, and GdNbO$_4$, respectively, and V is the volume fraction of GdNbO$_4$. The M–G model results are plotted in Fig. 7(b) and have a variation tendency similar to those of the measured thermal conductivities. All the experimental values are lower than the calculated values. It can be concluded that the ceramic composites, especially C1 and C2, have better thermal insulation properties than YSZ, making them beneficial for further application as new TBC materials.

3.5 Coefficients of thermal expansion

The deformation variation and CTEs of the Gd$_3$NbO$_7$/GdNbO$_4$ composites are plotted in Figs. 8(a) and 8(b). The CTEs of GdNbO$_4$ exhibit discontinuous variation, which has an abnormal decrease at 800 ℃ due to the phase transformation from the monoclinic phase to the tetragonal phase. The phase transition of GdNbO$_4$ is different from that of YSZ which is a first-order phase transition and generates sudden volume change. The

abrupt variation of volume will introduce extra stress to harm the thermal cycling lifetime of the thermal barrier coating [50]. In contrast, the phase transition of GdNbO$_4$ is a second-order phase transition, which has no abrupt volume change or extra stress [51]. Therefore, there is no harm in the thermal cycling lifetime of TBC. Such phase transition is reversible that the phase recovers when the temperature is lower than the phase-transition temperature. The CTEs of the Gd$_3$NbO$_7$/GdNbO$_4$ composites increase with increasing GdNbO$_4$ content below 1000 ℃, as shown in Fig. 8(c). Above 1000 ℃, the CTEs of tetragonal-GdNbO$_4$ lead to a decrease in the CTEs of the Gd$_3$NbO$_7$/GdNbO$_4$ composites. Moreover, the CTEs of the Gd$_3$NbO$_7$/GdNbO$_4$ composites gradually exhibit similar features to those of GdNbO$_4$, which show discontinuous variation at elevated temperatures with increasing GdNbO$_4$ content. The CTEs of Gd$_3$NbO$_7$/GdNbO$_4$ composites

are in the range of 8.7×10^{-6}–10.3×10^{-6} K^{-1}, which is comparable to those of YSZ (10.0×10^{-6}–10.5×10^{-6} K^{-1}, at 200–800 ℃) [42].

Several factors affect the CTEs of composite materials, including the crystal structure, imperfections, phase transformations, and thermal stresses. Assuming that there is no crack inside the samples and only uniform hydrostatic stresses exist in each phase, then the CTEs of the composites can be evaluated by Eq. (4):

$$A = \frac{\sum \dfrac{\alpha_i B_i F_i}{\rho_i}}{\sum \dfrac{B_i F_i}{\rho_i}} \tag{4}$$

where α_i, B_i, F_i, and ρ_i are the CTEs, the bulk modulus, the mass fraction, and the density of the *i*th phase in the composite, respectively. B can be calculated by Eq. (5):
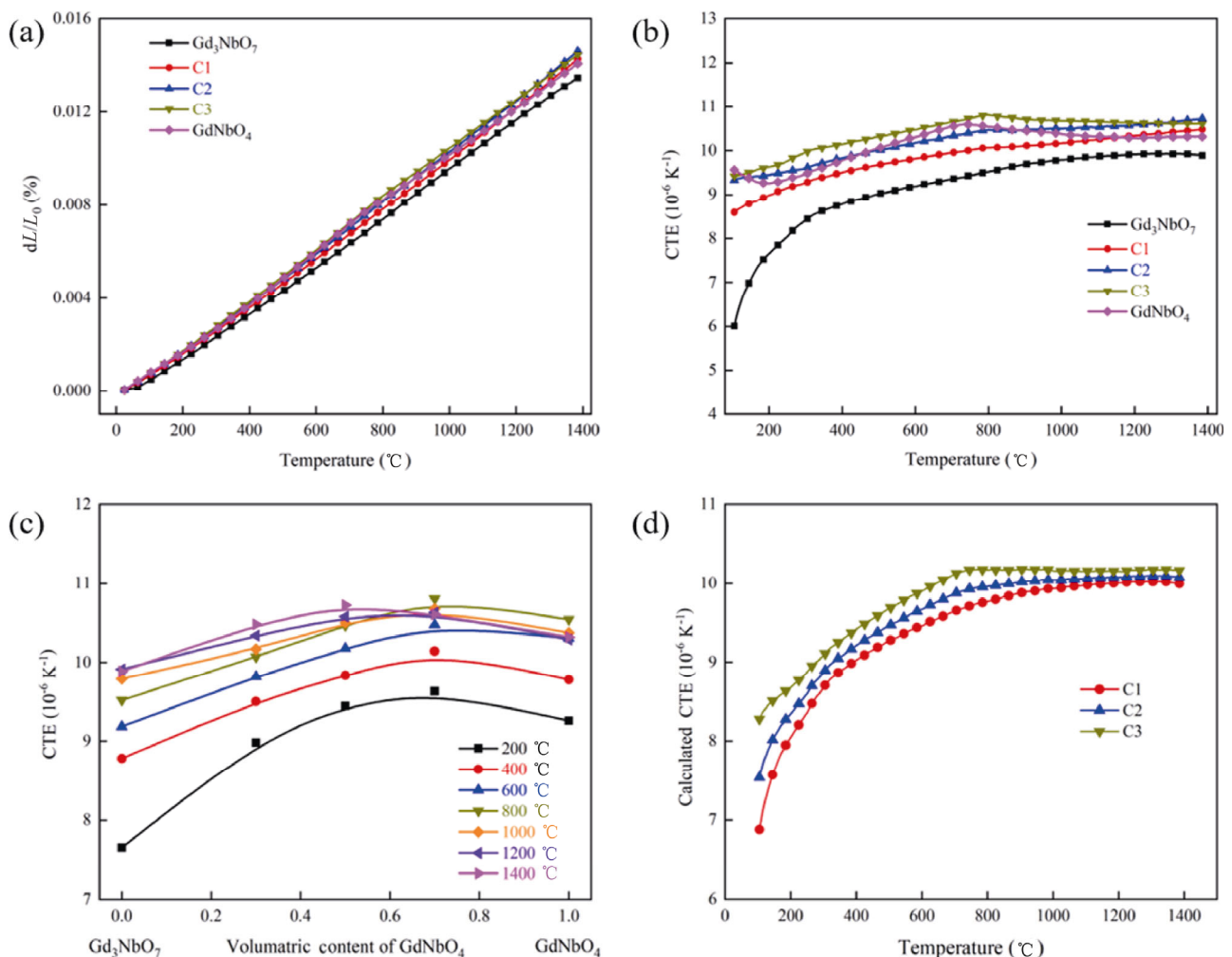

Fig. 8 Thermal expansion properties of Gd$_3$NbO$_7$/GdNbO$_4$ composites: (a) deformation variation and (b) measured CTEs. (c) CTEs as a function of GdNbO$_4$ content and (d) calculated CTEs.

$$B = \frac{E}{3(1-2\mu)} \tag{5}$$

where E and μ are the Young's modulus and the Poisson's ratio of each phase, respectively. Figures 8(b) and 8(d) show that the measured CTEs of the Gd_3NbO_7/ $GdNbO_4$ composites have variation tendencies similar to those of the calculated CTEs, which increase with increasing $GdNbO_4$ content. The calculated CTEs are somewhat lower than the measured CTEs because the calculation is carried out under relatively ideal conditions. Figure 8(c) shows that the CTEs for Gd_3NbO_7, C1, and C2 increase monotonically with increasing temperature. In this research, when the $GdNbO_4$ content is above 50 vol%, the CTEs of the ceramic composites do not increase monotonically at elevated temperatures. This finding may be due to either the suppression of phase transformation or the thermal expansion and volume variation, which counteract each other in the Gd_3NbO_7/$GdNbO_4$ composites with lower $GdNbO_4$ contents. The CTEs of the Gd_3NbO_7/$GdNbO_4$ composites are comparable to that of 8YSZ, indicating that the composites may have a small thermal stress and long thermal cycling life.

3. 6 Balanced mechanical and thermal properties

As the thermal conductivity and fracture toughness are considered the key thermal and mechanical properties of the TBC materials, a comparison between these two properties in this work and works from the literature is shown in Fig. 9. As the selection criteria of the TBC materials mostly rely on the low thermal conductivity
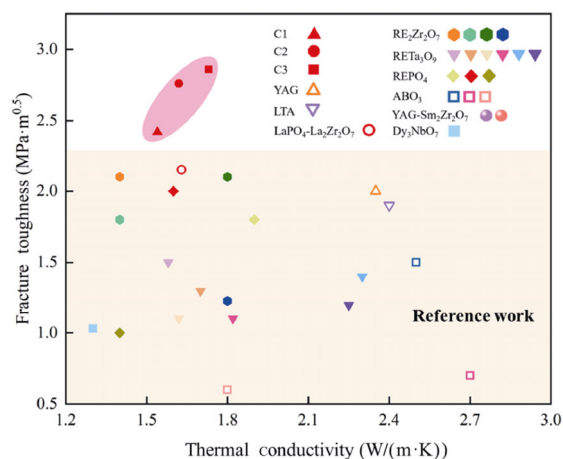
Fig. 9 Comparison of fracture toughness (room temperature) and thermal conductivity (800 ℃) between Gd_3NbO_7/$GdNbO_4$ composites and part of representative new materials as ceramic topcoat materials.

for the thermal insulation and the high fracture toughness for long cycling life, the materials in the upper left area in Fig. 9 are preferred for the TBCs. Compared with those reported in the representative reference works including both single-phase and composite materials, such as $RE_2Zr_2O_7$ [12–14], RE_3NbO_7 [26], $RETa_3O_9$ [29], $REPO_4$ [17], $SrZrO_3$ [21], $Ba(Mg_{1/3}Ta_{2/3})O_3$ [31], $LaPO_4$–$La_2Zr_2O_7$ [49], etc., the quasi-binary Gd_3NbO_7/$GdNbO_4$ composites in this work are much closer to the upper left area. Although $RE_2Zr_2O_7$ and RE_3NbO_7 as potential topcoat materials have a lower thermal conductivity, the weakness of fracture toughness influences their locations in Fig. 9. C2 and C3 have the best overall properties with balanced thermal conductivity and toughness.

4　Conclusions

This paper reports the quasi-binary $GdNbO_4$/Gd_3NbO_7 composites with balanced thermal and mechanical properties as a novel thermal barrier coating material. The quasi-binary composites show an enhanced fracture toughness, as the residual stress facilitates the ferroelastic domain switching, which is evidenced by the enlarged process zone and the increase in the crack deflection. The quasi-binary composites also show a low thermal conductivity due to the Gd_3NbO_7 phase, in which the large chemical inhomogeneity diffuses the phonons. As a result, Gd_3NbO_7/$GdNbO_4$ exhibits a balanced thermal conductivity of 1.6 W/(m·K) at 1073 K and a fracture toughness value of 2.76 MPa·m$^{0.5}$, which are among the best comprehensive properties that have been observed in new TBC materials. This quasi-binary composite can be synthesized *in-situ* from the Gd_2O_3 and Nb_2O_5 powders, thereby facilitating the fabrication of coatings through the thermal spray processing. The work demonstrates that the quasi-binary approach could be feasible for designing a novel material with the comprehensive properties required for the high-temperature TBCs.

Declaration of competing interest

The authors have no competing interests to declare that are relevant to the content of this article.

Electronic Supplementary Material

Supplementary material is available in the online version of this article at https://doi.org/10.1007/s40145-022-0622-2.

References

[1] Mercer C, Williams JR, Clarke DR, *et al*. On a ferroelastic mechanism governing the toughness of metastable tetragonal-prime (*t'*) yttria-stabilized zirconia. *Proc R Soc A* 2007, **463**: 1393–1408.

[2] Clarke DR, Oechsner M, Padture NP. Thermal-barrier coatings for more efficient gas-turbine engines. *MRS Bull* 2012, **37**: 891–898.

[3] Padture NP, Gell M, Jordan EH. Thermal barrier coatings for gas-turbine engine applications. *Science* 2002, **296**: 280–284.

[4] Padture NP. Advanced structural ceramics in aerospace propulsion. *Nat Mater* 2016, **15**: 804–809.

[5] Cao XQ, Vassen R, Stoever D. Ceramic materials for thermal barrier coatings. *J Eur Ceram Soc* 2004, **24**: 1–10.

[6] Saputra R, Walvekar R, Khalid M, *et al*. Synthesis and thermophysical properties of ethylammonium chloride–glycerol–$ZnCl_2$ ternary deep eutectic solvent. *J Mol Liq* 2020, **310**: 113232.

[7] Ren XR, Pan W. Mechanical properties of high-temperature-degraded yttria-stabilized zirconia. *Acta Mater* 2014, **69**: 397–406.

[8] Pan W, Phillpot SR, Wan CL, *et al*. Low thermal conductivity oxides. *MRS Bull* 2012, **37**: 917–922.

[9] Vaßen R, Jarligo MO, Steinke T, *et al*. Overview on advanced thermal barrier coatings. *Surf Coat Technol* 2010, **205**: 938–942.

[10] Clarke DR, Levi CG. Materials design for the next generation thermal barrier coatings. *Annu Rev Mater Res* 2003, **33**: 383–417.

[11] Zhu DM, Miller RA. Development of advanced low conductivity thermal barrier coatings. *Int J Appl Ceram Technol* 2005, **1**: 86–94.

[12] Xu Q, Pan W, Wang JD, *et al*. Rare-earth zirconate ceramics with fluorite structure for thermal barrier coatings. *J Am Ceram Soc* 2006, **89**: 340–342.

[13] Wan CL, Pan W, Xu Q, *et al*. Effect of point defects on the thermal transport properties of $(La_xGd_{1-x})_2Zr_2O_7$: Experiment and theoretical model. *Phys Rev B* 2006, **74**: 144109.

[14] Feng J, Xiao B, Wan CL, *et al*. Electronic structure, mechanical properties and thermal conductivity of $Ln_2Zr_2O_7$ (Ln = La, Pr, Nd, Sm, Eu and Gd) pyrochlore. *Acta Mater* 2011, **59**: 1742–1760.

[15] Curran JA, Kalkancı H, Magurova Y, *et al*. Mullite-rich plasma electrolytic oxide coatings for thermal barrier applications. *Surf Coat Technol* 2007, **201**: 8683–8687.

[16] Tian ZL, Zheng LY, Wang JM, *et al*. Theoretical and experimental determination of the major thermo–mechanical properties of RE_2SiO_5 (RE = Tb, Dy, Ho, Er, Tm, Yb, Lu, and Y) for environmental and thermal barrier coating applications. *J Eur Ceram Soc* 2016, **36**: 189–202.

[17] Du AB, Wan CL, Qu ZX, *et al*. Thermal conductivity of monazite-type $REPO_4$ (RE = La, Ce, Nd, Sm, Eu, Gd). *J Am Ceram Soc* 2009, **92**: 2687–2692.

[18] Xie XY, Guo HB, Gong SK, *et al*. Lanthanum–titanium–aluminum oxide: A novel thermal barrier coating material for applications at 1300 ℃. *J Eur Ceram Soc* 2011, **31**: 1677–1683.

[19] Zhang P, Choy KL. The synthesis of thermochemically stable single phase lanthanum titanium aluminium oxide. *Ceram Int* 2016, **42**: 3261–3267.

[20] Gadow R, Lischka M. Lanthanum hexaaluminate—novel thermal barrier coatings for gas turbine applications—materials and process development. *Surf Coat Technol* 2002, **151–152**: 392–399.

[21] Ma W, Mack DE, Vaßen R, *et al*. Perovskite-type strontium zirconate as a new material for thermal barrier coatings. *J Am Ceram Soc* 2008, **91**: 2630–2635.

[22] Shian S, Sarin P, Gurak M, *et al*. The tetragonal–monoclinic, ferroelastic transformation in yttrium tantalate and effect of zirconia alloying. *Acta Mater* 2014, **69**: 196–202.

[23] Limarga AM, Shian S, Leckie RM, *et al*. Thermal conductivity of single- and multi-phase compositions in the ZrO_2–Y_2O_3–Ta_2O_5 system. *J Eur Ceram Soc* 2014, **34**: 3085–3094.

[24] Pitek FM, Levi CG. Opportunities for TBCs in the ZrO_2–$YO_{1.5}$–$TaO_{2.5}$ system. *Surf Coat Technol* 2007, **201**: 6044–6050.

[25] Yang J, Pan W, Han Y, *et al*. Mechanical properties, oxygen barrier property, and chemical stability of RE_3NbO_7 for thermal barrier coating. *J Am Ceram Soc* 2020, **103**: 2302–2308.

[26] Guo L, Yan Z, Dong X, *et al*. Composition-microstructure-mechanical property relationships and toughening mechanisms of $GdPO_4$-doped $Gd_2Zr_2O_7$ composites. *Compos B: Eng* 2019, **161**: 473–482.

[27] Wang CM, Guo L, Zhang Y, *et al*. Enhanced thermal expansion and fracture toughness of Sc_2O_3-doped $Gd_2Zr_2O_7$ ceramics. *Ceram Int* 2015, **41**: 10730–10735.

[28] Chen L, Jiang YH, Chong XY, *et al*. Synthesis and thermophysical properties of $RETa_3O_9$ (RE = Ce, Nd, Sm, Eu, Gd, Dy, Er) as promising thermal barrier coatings. *J Am Ceram Soc* 2018, **101**: 1266–1278.

[29] Du AB, Pan W, Ahmad K, *et al*. Enhanced mechanical properties of machinable $LaPO_4$/Al_2O_3 Composites by spark plasma sintering. *Int J Appl Ceram Technol* 2009, **6**: 236–242.

[30] Ma W, Jarligo MO, Mack DE, *et al*. New generation

perovskite thermal barrier coating materials. *J Therm Spray Technol* 2008, **17**: 831–837.

[31] Rödel J, Kelly JF, Lawn BR. *In situ* measurements of bridged crack interfaces in the scanning electron microscope. *J Am Ceram Soc* 1990, **73**: 3313–3318.

[32] Zhang P, Feng YJ, Li Y, *et al*. Thermal and mechanical properties of ferroelastic RENbO$_4$ (RE = Nd, Sm, Gd, Dy, Er, Yb) for thermal barrier coatings. *Scripta Mater* 2020, **180**: 51–56.

[33] Adachi T, Sekino T, Nakayama T, *et al*. Measurement of microscopic stress distribution of multilayered composite by X-ray stress analysis. *Mater Lett* 2003, **57**: 3057–3062.

[34] Shokrieh MM, Ghanei Mohammadi AR. 3-Nondestructive testing (NDT) techniques in the measurement of residual stresses in composite materials: An overview. In: *Residual Stresses in Composite Materials*, 2nd edn. Woodhead Publishing, 2021: 71–109.

[35] Prevey PS. X-ray diffraction residual stress techniques. In: *Materials Characterization*. ASM International, 1986: 380–392.

[36] Roytburd AL, Ouyang J, Artemev A. Polydomain structures in ferroelectric and ferroelastic epitaxial films. *J Phys: Condens Matter* 2017, **29**: 163001.

[37] Roitburd AL. Equilibrium structure of epitaxial layers. *Phys Stat Sol* (*a*) 1976, **37**: 329–339.

[38] Ayatollahi MR, Zakeri M. An improved definition for mode I and mode II crack problems. *Eng Fract Mech* 2017, **175**: 235–246.

[39] Davidge RW, Green TJ. The strength of two-phase ceramic/glass materials. *J Mater Sci* 1968, **3**: 629–634.

[40] Agar JC, Damodaran AR, Okatan MB, *et al*. Highly mobile ferroelastic domain walls in compositionally graded ferroelectric thin films. *Nat Mater* 2016, **15**: 549–556.

[41] Yang J, Han Y, Shahid M, *et al*. A promising material for thermal barrier coating: Pyrochlore-related compound Sm$_2$FeTaO$_7$. *Scripta Mater* 2018, **149**: 49–52.

[42] Feng J, Xiao B, Zhou R, *et al*. Thermal expansion and conductivity of RE$_2$Sn$_2$O$_7$ (RE = La, Nd, Sm, Gd, Er and Yb) pyrochlores. *Scripta Mater* 2013, **69**: 401–404.

[43] Zhao M, Ren XR, Yang J, *et al*. Low thermal conductivity of rare-earth zirconate–stannate solid solutions (Yb$_2$Zr$_2$O$_7$)$_{1-x}$ (Ln$_2$Sn$_2$O$_7$)$_x$ (Ln = Nd, Sm). *J Am Ceram Soc* 2016, **99**: 293–299.

[44] Wang YJ, Zhang L, Wu WJ, *et al*. Enhancement of thermal properties of ytterbium–cerium oxide by zirconium doping for thermal barrier coatings. *Philos Mag Lett* 2019, **99**: 309–316.

[45] Lehmann H, Pitzer D, Pracht G, *et al*. Thermal conductivity and thermal expansion coefficients of the lanthanum rare-earth-element zirconate system. *J Am Ceram Soc* 2003, **86**: 1338–1344.

[46] Chen L, Wu P, Song P, *et al*. Potential thermal barrier coating materials: RE$_3$NbO$_7$ (RE = La, Nd, Sm, Eu, Gd, Dy) ceramics. *J Am Ceram Soc* 2018, **101**: 4503–4508.

[47] Yang J, Qian X, Pan W, *et al*. Diffused lattice vibration and ultralow thermal conductivity in the binary Ln–Nb–O oxide system. *Adv Mater* 2019, **31**: e1808222.

[48] Yang J, Wan CL, Zhao M, *et al*. Effective blocking of radiative thermal conductivity in La$_2$Zr$_2$O$_7$/LaPO$_4$ composites for high temperature thermal insulation applications. *J Eur Ceram Soc* 2016, **36**: 3809–3814.

[49] Vassen R, Stuke A, Stöver D. Recent developments in the field of thermal barrier coatings. *J Therm Spray Technol* 2009, **18**: 181–186.

[50] Sarin P, Hughes RW, Lowry DR, *et al*. High-temperature properties and ferroelastic phase transitions in rare-earth niobates (LnNbO$_4$). *J Am Ceram Soc* 2014, **97**: 3307–3319.

[51] Mendelson MI. Average grain size in polycrystalline ceramics. *J Am Ceram Soc* 1969, **52**: 443–446.

[52] Taya M, Hayashi S, Kobayashi AS, *et al*. Toughening of a particulate-reinforced ceramic-matrix composite by thermal residual stress. *J Am Ceram Soc* 1990, **73**: 1382–1391.

[53] Ren XR, Guo SC, Zhao M, *et al*. Thermal conductivity and mechanical properties of YSZ/LaPO$_4$ composites. *J Mater Sci* 2014, **49**: 2243–2251.

[54] Du LF, Yang SM, Zhang P, *et al*. Pinning effect of different shape second-phase particles on grain growth in polycrystalline: Numerical and analytical investigations. *Compos Interfaces* 2018, **25**: 357–368.